The Astrophysical Journal, 916:109 (15pp), 2021 August 1 https://doi.org/10.3847/1538-4357/ac06c6

The Growth of Protoplanets via the Accretion of Small Bodies in Disks Perturbed by the Planetary Gravity

Tatsuya Okamura and Hiroshi Kobayashi
Department of Physics, Nagoya University, Nagoya, Aichi 464-8602, Japan; okamura.tatsuya@nagoya-u.jp
Received 2021 April 22; revised 2021 May 21; accepted 2021 May 30; published 2021 August 4

Abstract

Planets grow via the collisional accretion of small bodies in a protoplanetary disk. Such small bodies feel strong gas drag, and their orbits are significantly affected by the gas flow and atmospheric structure around the planet. We investigate the gas flow in the protoplanetary disk perturbed by the gravity of the planet by 3D hydrodynamical simulation. We then calculate the orbital evolutions of particles in the gas structure obtained from the hydrodynamical simulation. Based on the orbital calculations, we obtain the collision rate between the planet and centimeter-to-kilometer-sized particles. Our results show that meter-sized or larger particles effectively collide with the planet owing to the atmospheric gas drag, which significantly enhances the collision rate. On the other hand, the gas flow plays an important role for smaller particles. Finally, considering the effects of the atmosphere and gas flow, we derive the new analytic formula for the collision rate, which is in good agreement with our simulations. We estimate the growth timescale and accretion efficiency of drifting bodies for the formation of a gas giant solid core using the formula. We find that the accretion of sub-kilometer-sized bodies achieves a short growth timescale ($\sim$0.05 Myr) and a high accretion efficiency ($\sim$1) for the core formation at 5 au in the minimum-mass solar nebula model.

Unified Astronomy Thesaurus concepts: Planet formation (1241); Protoplanetary disks (1300)

1. Introduction

In the past 10 yr, the growth of protoplanets is considered via the accretion of millimeter-to-centimeter-sized particles (pebbles), as well as kilometer-sized planetesimals (e.g., Ormel & Klahr 2010; Lambrechts & Johansen 2012). Pebbles, formed from dust grain coagulation, drift inward and are effectively accreted onto protoplanets in inner protoplanetary disks. These pebbles are aerodynamically small and well coupled to the gas, so that the gas flow significantly affects the collision rate between pebbles and planets. Recently, the detailed flow structures around a low-mass and non-gap-opening planet embedded in a protoplanetary disk were revealed by hydrodynamical simulations (Fung et al. 2015, 2019; Ormel et al. 2015b; Cimerman et al. 2017; Lambrechts & Lega 2017; Kurokawa & Tanigawa 2018; Béthune & Rafikov 2019; Kuwahara et al. 2019; Moldenhauer et al. 2021). The common flow structures of these studies are the horseshoe and vertical flow. The horseshoe flow extends along the orbital direction of the planet in the anterior−posterior direction of the planet and has a vertical structure like a column. The vertical flow comes from high altitudes to planets. These flow structures influence the collision rate between pebbles and the planet (Ormel 2013). Popovas et al. (2018, 2019) showed that the horseshoe flow takes pebbles away from the planet and prevents the particles from accreting onto the planet. Kuwahara & Kurokawa (2020a) showed that the vertical flow helps small particles accreting onto the planet, so that the collision rate increases if pebbles have a vertical distribution. The analytic formula for the collision rates with planets has been derived for particles well coupled to the gas (Ormel & Klahr 2010; Ormel 2013).

On the other hand, the planetary atmosphere enhances the accretion rate of meter-sized or larger bodies. Once protoplanets grow larger than the Moon, they can have atmospheres (e.g., Mizuno et al. 1978). The gas density of the atmosphere may be orders of magnitude larger than the protoplanetary disk. In addition, a close encounter with a planet accelerates the velocity of particles, and the velocity may exceed the speed of sound. These effects effectively reduce the kinetic energy of particles so that the particles are captured in the atmosphere. The effective capture radius for sub-kilometer-sized bodies is much larger than the physical radius of the planet (Inaba & Ikoma 2003). For the accretion rate, Inaba & Ikoma (2003) derived the analytic formula, which is valid for accretion of sub-kilometer-sized or larger particles. However, their formula overestimates the accretion rate of the meter-sized or smaller particles because the effective capture radius is estimated to be comparable to the Hill radius of the planet. Therefore, the atmosphere structure and flow around a protoplanet are necessary to derive accretion rates of centimeter-to-kilometer-sized particles consistently.

Kurokawa & Tanigawa (2018) showed, by hydrodynamical simulation, that the atmospheric structure isolated from the protoplanetary disk is formed around the planet owing to the cooling. Therefore, the self-consistent flow and atmosphere around a planet are obtainable via hydrodynamic simulation. The accretion rate of bodies from pebbles to planetesimals can be calculated via the orbital simulation of bodies based on the density and velocity profile in the disk obtained via the hydrodynamical simulation. Such combined simulations were carried out only for meter-sized or smaller particles (Popovas et al. 2018, 2019; Kuwahara & Kurokawa 2020a, 2020b). However, the accretion rate for a wide size range of particles is helpful to discuss the dominant accreted bodies onto a planet.

In this paper, we investigate the collision rate between small bodies and a planet in the protoplanetary disk perturbed by the planetary gravity. Our goal is to find out the effects of the gas flow and planetary atmosphere on the collision rate. We perform hydrodynamical simulations and orbital calculations of centimeter-to-kilometer-sized particles in the gas flow obtained from the hydrodynamical simulation. Based on simulations, we

derive the new analytic formula for the collision rate in the disk perturbed by the planetary gravity, including the gas flow and planetary atmosphere. In Section 2, we describe the simulation methods for hydrodynamics and orbital evolution of particles. In Section 3, we show the gas flow and atmospheric structure around a planet given by the hydrodynamical simulation and obtain the collision rate between the planet and particles via orbital calculation. In Section 4, we derive the new analytic formulae for the collision rate. In Sections 5 and 6, we discuss and summarize our findings.

2. Methods

2.1. Hydrodynamical Simulations

2.1.1. Basic Equations

We investigate the gas flow around a protoplanet with a circular orbit of radius a in a protoplanetary disk around the host star with mass M_* via hydrodynamical simulation. We assume a compressible, inviscid, nonisothermal, non-self-gravitating fluid. The basic equations of the hydrodynamical simulations are the equation of continuity, the Euler equation, and the energy conservation equation, given by

$$\frac{\partial \rho_g}{\partial t} + \nabla \cdot (\rho_g \boldsymbol{v}_g) = 0, \tag{1}$$

$$\left(\frac{\partial}{\partial t} + \boldsymbol{v}_g \cdot \nabla\right)\boldsymbol{v}_g = -\frac{\nabla p}{\rho_g} + (\boldsymbol{F}_{cor} + \boldsymbol{F}_{tid} + \boldsymbol{F}_p), \tag{2}$$

$$\frac{\partial E}{\partial t} + \nabla \cdot [(E + p)\boldsymbol{v}_g] = \rho_g \boldsymbol{v}_g \cdot (\boldsymbol{F}_{cor} + \boldsymbol{F}_{tid} + \boldsymbol{F}_p) - \frac{U(\rho_g, T) - U(\rho_g, T_0)}{\beta/\Omega}, \tag{3}$$

where ρ_g is the gas density; $\boldsymbol{v}_g$ is the gas velocity; p is the pressure; $\boldsymbol{F}_{cor}$ is the Coriolis force; $\boldsymbol{F}_{tid}$ is the tidal force; $\boldsymbol{F}_p$ is the gravitational force; Ω is the orbital frequency; β is the dimensionless cooling timescale; T and T_0 are the fluid and background temperatures, respectively; and U and E are, respectively, the internal and total energy densities, given by

$$U = \frac{p}{\gamma - 1}, \tag{4}$$

$$E = U + \frac{1}{2}\rho_g v_g^2, \tag{5}$$

with the ratio of specific heat $\gamma = 7/5$.

The forces in Equations (2) and (3) are given by $\boldsymbol{F}_{cor} = -2\Omega \boldsymbol{e}_z \times \boldsymbol{v}_g$, $\boldsymbol{F}_{tid} = 3x\Omega^2 \boldsymbol{e}_x - z\Omega^2 \boldsymbol{e}_z$, and

$$\boldsymbol{F}_p = \nabla\left(\frac{GM_p}{\sqrt{r^2 + r_s^2}}\right)\left\{1 - \exp\left[-\frac{1}{2}\left(\frac{t}{t_{inj}}\right)^2\right]\right\}, \tag{6}$$

where $\boldsymbol{e}_i$ is the unit vector in the i-direction, M_p is the mass of the planet, G is the gravitational constant, r is the distance from the center of the planet, r_s is the softening length, and t_{inj} is the injection time of planetary gravity. To avoid the numerical effect, the gravity of the planet is gradually inserted using the injection time $t_{inj} = 0.5\Omega^{-1}$ (Ormel et al. 2015a). The planet has an atmosphere with radius $\sim R_B$, where $R_B \equiv GM_p/c_s^2$ is the Bondi radius and c_s is the isothermal sound speed. To resolve the atmospheric structure, we set $r_s = 0.1R_B$ according to Kurokawa & Tanigawa (2018).

The last term in Equation (3) is the cooling function according to the β cooling model, where the temperature T relaxes toward T_0 in the timescale β/Ω (e.g., Gammie 2001). In this study, we adopt the β cooling model to obtain the density profile and flow around the planetary atmosphere according to Kurokawa & Tanigawa (2018), who showed that the atmosphere is formed around the planet using the β cooling model. We set $\beta = (R_B\Omega/0.1c_s)^2$ according to the previous studies (Kurokawa & Tanigawa 2018; Kuwahara & Kurokawa 2020a, 2020b).

The time, velocity, and length are considered to be normalized by the reciprocal of the Keplerian orbital frequency Ω^{-1}, the isothermal sound speed c_s, and the gas scale height $H \equiv c_s/\Omega$, respectively. The basic equations are then characterized by a dimensionless number, given by

$$m = \frac{R_B}{H} = \frac{GM_p\Omega}{c_s^3}. \tag{7}$$

The Hill radius is written as a function of m:

$$R_H = \left(\frac{m}{3}\right)^{1/3} H. \tag{8}$$

We assume a solar-mass host star and a disk temperature profile $T = 270(a/1\ \text{au})^{-1/2}$ (i.e., the minimum-mass solar nebula model; Weidenschilling 1977a; Hayashi et al. 1985), so that M_p is given by (Kurokawa & Tanigawa 2018)

$$M_p \simeq 12m\left(\frac{a}{1\ \text{au}}\right)^{3/4} M_\oplus. \tag{9}$$

We investigate the cases with $m = 0.1$, 0.05, and 0.03, which correspond to $M_p/M_\oplus = 1.2$ (4.0), 0.6 (2.0), and 0.36 (1.2) at 1 (5) au, respectively.

2.1.2. Simulation Setups and Boundary Conditions

In this study, we use the hydrodynamical simulation code Athena++ (White et al. 2016; Stone et al. 2020). We choose the HLLC algorithm for a Riemann solver. Our simulations are performed in a spherical−polar coordinate (r, θ, ϕ) centered on the planet. We focus on the embedded, non-gap-opening regime, and thus the local simulations are likely to be valid. In order to resolve the flow structure around the planet in detail, we adopt a logarithmic grid for the radial dimension. In the polar angle direction, the cell size is proportional to $(3\psi^2 + 1)$, where ψ is the angle from the midplane. The cell spacing near the midplane is smaller than near the pole (i.e., resolution near the midplane is higher than near the pole; Kurokawa & Tanigawa 2018). The numerical resolution is set to be $128 \times 64 \times 128$ in the r, θ, and ϕ directions, respectively. The computational domain ranges from 0 to 2π for ϕ, from 0 to π for θ, and from r_{inn} to r_{out} for r, where r_{inn} and r_{out} are the radii at the inner and outer boundaries, respectively.

We assume that the initial and outer boundary values in hydrodynamical simulations are those of a Kepler disk without

Table 1
List of Parameters for Our Simulations

m	Physical Mass ($M_\oplus$)	R_B (H)	R_H (H)	r_{inn} (H)	r_{out} (H)	t_{end} (Ω^{-1})	β
0.03	0.36	0.03	0.22	9.32×10^{-4}	0.5	50	0.09
0.05	0.6	0.05	0.26	1.1×10^{-3}	0.75	100	0.25
0.1	1.2	0.1	0.32	1.39×10^{-3}	5	150	1

Note. The first column shows the value of dimensionless mass of the planet. The second to eighth columns represent the corresponding values at 1 au for the mass of the planet normalized by the Earth mass, the Bondi radius, the Hill radius, the size of the inner boundary, the size of the outer boundary, termination time of the hydrodynamical simulation, and dimensionless cooling timescale β.

a pressure gradient term, therefore given by

$$\rho_{g,0} = \rho_0 \exp\left[-\frac{1}{2}\left(\frac{z}{H}\right)^2\right], \tag{10}$$

$$\boldsymbol{v}_{g,0} = -\frac{3}{2}\Omega x \boldsymbol{e}_y, \tag{11}$$

where ρ_0 is the density at the midplane and z is the distance from the midplane. We focus on the shear regime of pebble accretion, where the shear velocity is more dominant than the headwind of the gas to determine the accretion rate. The condition satisfied to be in the shear regime is given by (Ormel 2017)

$$M_p \gg \frac{1}{8}\frac{v_{hw}^3}{G\Omega \mathrm{St}_0} \simeq 2.0 \times 10^{-4} M_\oplus \frac{1}{\mathrm{St}_0}\left(\frac{a}{1\ \mathrm{au}}\right)^{3/2}\left(\frac{v_{hw}}{50\ \mathrm{m\ s^{-1}}}\right)^3, \tag{12}$$

where v_{hw} is the headwind of the gas and St_0 is the dimensionless stopping time of a particle (see Equation (18)). We perform simulations for $M_p = 0.36 - 1.2\, M_\oplus$ at $a = 1$ au ($M_p = 1.2 - 4.0\, M_\oplus$ at $a = 5$ au) and $\mathrm{St}_0 = 3.0 \times 10^{-3}$ to 1.0×10^{13}, so that we ignore the headwind in our simulations.

We set the radius of the inner boundary according to that of the planet (Kuwahara & Kurokawa 2020a). We assume the density of the planet $\rho_{pl} = 5\ \mathrm{g\ cm^{-3}}$, so that the radius of the inner boundary is given by

$$r_{inn} = \left(\frac{3M_p}{4\pi\rho_{pl}}\right)^{1/3} = \left(\frac{9M_*}{4\pi\rho_{pl}}\right)^{1/3}\frac{R_H}{a} \simeq 3 \times 10^{-3} m^{1/3}\left(\frac{\rho_{pl}}{5\ \mathrm{g\ cm^{-3}}}\right)^{-1/3} \times \left(\frac{M_*}{1M_\odot}\right)^{1/3}\left(\frac{a}{1\ \mathrm{au}}\right)^{-1}. \tag{13}$$

We introduce the reflective boundary condition for the inner boundary, but Kurokawa & Tanigawa (2018) reported that this condition generates the unphysical energy flow in the results of simulations by Athena++. In order to prevent this unphysical affair from affecting the entire flow, we introduce the artificial cooling at the three inner cells ($\beta = 10^{-5}$; Kurokawa & Tanigawa 2018). The boundary condition in the azimuthal direction is set to the periodic boundary, which means that $A(r, \theta, \phi) = A(r, \theta, \phi + 2\pi)$ holds for an arbitrary physical quantity A. We calculate until the steady-state flow is almost achieved at $t = t_{end}$. We set t_{end} according to Kuwahara & Kurokawa (2020a). A summary of our simulation parameters is shown in Table 1, which are chosen from the values at $a = 1$ au.

2.2. Orbital Calculations

2.2.1. Equations and Gas Drag Law

We calculate orbits of particles in the gas flow obtained from hydrodynamical simulations. The equation of motion of the particle is given by

$$\frac{d\boldsymbol{v}}{dt} = \begin{pmatrix} 2v_y\Omega + 3x\Omega^2 \\ -2v_x\Omega \\ -z\Omega^2 \end{pmatrix} - \frac{GM_p}{r^3}\begin{pmatrix} x \\ y \\ z \end{pmatrix} + \frac{\boldsymbol{F}_{drag}}{m_p}, \tag{14}$$

where $\boldsymbol{v} = (v_x, v_y, v_z)$ is the velocity vector of the particle, $\boldsymbol{r} = (x, y, z)$ is its position vector with respect to the center of the planet, and m_p is the mass of the particle. The first and second terms on the right-hand side of Equation (14) are the Coriolis and tidal forces and the gravity force of the planet, respectively. The third term is the gas drag force given by (e.g., Adachi et al. 1976)

$$\boldsymbol{F}_{drag} = -\frac{C_D}{2}\pi r_p^2 \rho_g u \boldsymbol{u}, \tag{15}$$

where r_p is a particle radius, $\boldsymbol{u} \equiv \boldsymbol{v} - \boldsymbol{v}_g$, $u = |\boldsymbol{u}|$ is the velocity of a particle relative to the gas, and C_D is the gas drag coefficient. We consider centimeter-to-kilometer-sized particles; C_D is given by the Stokes gas drag for small particles, while C_D is constant for large particles (Adachi et al. 1976). In addition, if particle velocities exceed the sound speed due to planetary gravity, the supersonic gas drag law should be applied. The gas drag coefficient, C_D, is approximated to be (Adachi et al. 1976; Tanigawa et al. 2014)

$$C_D = \frac{12\nu}{r_p u} + \frac{(2 - w)M}{1.6 + M} + w, \tag{16}$$

where ν is the kinetic viscosity, $M \equiv u/c_s$ is the Mach number, and $w = 0.4$ is the correction factor. In Equation (16), the first, second, and third terms indicate Stokes, quadratic, and supersonic drag coefficients, respectively, and we ignore Epstein drag for simplicity. In our simulation, we do not consider the evaporation or ablation. The kinetic viscosity is given by $\nu = l_{mfp}c_s/2$, where $l_{mfp} = \mu m_H/\rho_g\sigma$ is the mean free path of the gas, $\mu = 2.34$ is the mean molecular weight, $m_H = 1.67 \times 10^{-24}$ g is the mass of the proton, and $\sigma = 2 \times 10^{-15}\ \mathrm{cm^2}$ is the molecular collision cross section (Chapman & Cowling 1970; Adachi et al. 1976). The stopping

time of a particle is expressed by

$$t_{\rm stop} = \frac{m_{\rm p} u}{|\boldsymbol{F}_{\rm drag}|} = \frac{4\rho_{\rm p} r_{\rm p}^2}{9\rho_{\rm g} c_{\rm s} l_{\rm mfp}}\left(1 + \frac{2M + 1.6w}{1.6 + M}\cdot\frac{r_{\rm p} u}{6 c_{\rm s} l_{\rm mfp}}\right)^{-1}, \tag{17}$$

where $\rho_{\rm p}$ is the density of a particle. We investigate the orbits of particles with different radii. We introduce the Stokes parameter, St, defined as the stopping time multiplied by Ω. The initial particle has $u \ll c_{\rm s}$, so that the gas drag is mainly given in the Stokes gas drag regime. This initial Stokes parameter is approximated to be

$$\mathrm{St}_0 = 4.5 \times 10^{-4}\left(\frac{\rho_{\rm p}}{1\ \mathrm{g\ cm^{-3}}}\right) \times \left(\frac{c_{\rm s}}{1\ \mathrm{km\ s^{-1}}}\right)^{-1}\left(\frac{r_{\rm p}}{1\ \mathrm{cm}}\right)^2, \tag{18}$$

where the value of $c_{\rm s}$ is chosen as that approximately at 1 au in the minimum-mass solar nebula model. Note that St continuously changes during the calculation. The value of St can be less than St_0 owing to the gas drag for $u \gg c_{\rm s}$. We use St_0 given in Equation (18) as a parameter instead of the radii of particles.

2.2.2. Numerical Setups: 3D Orbital Calculations

A particle is launched from a starting point ($x_{\rm s}$, $y_{\rm s}$, $z_{\rm s}$), where $y_{\rm s}$ is fixed at $y_{\rm s} = 40\,R_{\rm H}$, and $x_{\rm s}$ and $z_{\rm s}$ are varied (Ida & Nakazawa 1989; Ormel & Klahr 2010). The particle is initially well coupled to the gas for $\mathrm{St}_0 \ll 1$, while the motion is determined by Kepler's laws for $\mathrm{St}_0 \gg 1$. We thus set the initial condition according to the gas motion for $\mathrm{St}_0 < 1$ or the orbital elements for $\mathrm{St}_0 > 1$. If the orbital eccentricities of particles are much smaller than the Hill radius of the planet divided by a, the collision rate is independent of eccentricities (Ida & Nakazawa 1989). We set initially circular orbits. The initial conditions are given as follows:

$$z_{\rm s} = \begin{cases} z_0 & (\mathrm{St}_0 < 1), \\ i a_{\rm s} \sin\omega \equiv z_0 \sin\omega & (\mathrm{St}_0 > 1), \end{cases}$$
$$\boldsymbol{v}_0 = \left(0,\ -\frac{3}{2}\Omega x_{\rm s},\ v_{z,0}\right),$$
$$v_{z,0} = \begin{cases} 0 & (\mathrm{St}_0 < 1), \\ z_0 \cos\omega & (\mathrm{St}_0 > 1), \end{cases} \tag{19}$$

where i is the initial inclination of the particle, $a_{\rm s}$ is its initial semimajor axis, and ω is its longitude of ascending node. We assume that ω is distributed uniformly in the range between 0 and π and take the average for the calculation of the collision rate. For $\mathrm{St}_0 < 1$, we ignore the z-component of the tidal force in Equation (14) assuming the balance with turbulent stirring according to Kuwahara & Kurokawa (2020a, 2020b).

The lower limits of $x_{\rm s}$ and z_0 are set to $x_{\rm s} = 0.0001H$ and $z_0 = 0$, and the spatial intervals of $x_{\rm s}$ and z_0 are $0.0001H$ and $0.02H$. The upper limits of $x_{\rm s}$ and z_0 are set to a few disk scale heights. We calculate orbits only coming from positive x and y because of the symmetry.

We use $\rho_{\rm g}$, $\boldsymbol{v}_{\rm g}$, and $c_{\rm s}$ given from the hydrodynamical simulation at $t = t_{\rm end}$, at which the fluid is in a quasi-steady state. The starting point of the particle is out of the computational domain of our hydrodynamical simulation ($r_{\rm out}$), so that we set the velocity and density of gas in $r > r_{\rm out}$ the same as the outer boundary conditions given in Equations (10) and (11). In our hydrodynamical simulations for $m = 0.03$ and $m = 0.05$, unexpected vortices appear in the horseshoe structure. These vortices are found by Kuwahara & Kurokawa (2020a, 2020b), which are caused by the low resolution of the distant place from the planet. In these cases, we only use the results of the hydrodynamical simulation in $r < 0.3H$ ($m = 0.03$) and in $r < 0.55H$ ($m = 0.05$), respectively. All physical quantities obtained via hydrodynamical simulations are the discrete data, so that we interpolate physical quantities using the linear interpolation method (Kuwahara & Kurokawa 2020a).

Orbital integration is terminated if any one of the following conditions is satisfied: (i) a particle goes far away, $|y| > 40\,R_{\rm H}$.; or (ii) a particle collides with the planet, $r < r_{\rm inn}$, where $r_{\rm inn}$ is the inner boundary for hydrodynamical simulations and the physical radius of the planet in Equation (13).

We numerically integrate Equation (14) using the Runge–Kutta–Fehlberg scheme (Fehlberg 1969; Eshagh 2005; Ormel & Klahr 2010). This integration method controls each time step comparing a fourth-order solution with a fifth-order solution. We set the relative error tolerance of 10^{-8}, which ensures numerical convergence (Ormel & Klahr 2010; Visser & Ormel 2016).

We show the sketch of the orbital calculation of particles in Figure 1.

3. Results of Simulations

3.1. Hydrodynamical Simulation

Figures 2 and 3 show the flow structures in the midplane ($z = 0$) and in the plane of $y = 0$ at $t = t_{\rm end}$, respectively. The additional simulations for $t > t_{\rm end}$ show that the flow structure and physical quantities almost keep constant subsequent to $t = t_{\rm end}$, so that the fluid is in a quasi-steady state. The characteristic structures of the gas flow formed in the simulations are similar to the previous studies (Fung et al. 2015, 2019; Ormel et al. 2015b; Cimerman et al. 2017; Lambrechts & Lega 2017; Kurokawa & Tanigawa 2018; Popovas et al. 2018; Béthune & Rafikov 2019; Chrenko & Lambrechts 2019; Kuwahara et al. 2019). These structures are divided into four parts: (i) The Keplerian shear streams exist in a distant place from the planet ($|x| \gtrsim 0.4H$ in Figure 2). These streamlines are almost same as the initial and outer boundary conditions, because the planet is too far to change the flow. (ii) The horseshoe flow extends along the orbital direction of the planet in the anterior−posterior direction of the planet. The U-turn flows caused by the horseshoe flow are seen in $|x| \lesssim 0.1H$ and $|y| \gtrsim 0.2H$ in Figure 2. (iii) The vertical flow comes from high altitudes to planets, as seen in $|x| \lesssim 0.1H$ and $|z| \gtrsim 0.1H$ in Figure 3. Of course, this result is specific to 3D calculations. (iv) The atmospheric structure is formed around the planet, as seen in $|r| \lesssim 0.1H$ in Figures 2 and 3. This region is isolated from the outer flow, which means that the gas recycling does not occur. This isolated envelope is formed owing to the cooling (Kurokawa & Tanigawa 2018).

To see the atmospheric density profile, we plot the density profile averaged over the azimuthal direction (ϕ) in the midplane (Figure 4). The density at $r < 0.1H$ significantly increases with decreasing r, while the radial density slope at $r \lesssim 4 \times 10^{-3}H$ becomes shallower owing to the softening. In a

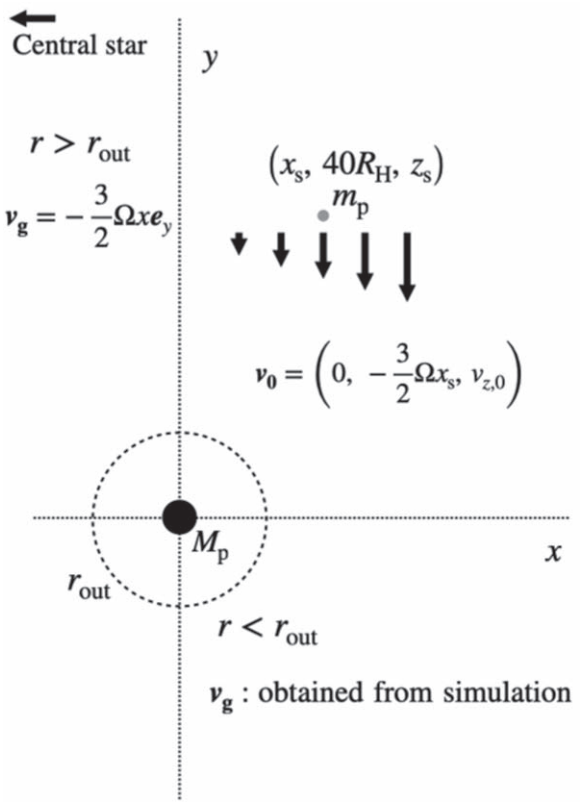

Figure 1. Sketch of the orbital calculation of particles in the corotating frame. A planet is located at the origin of the frame. We calculate orbits only coming from positive x and y because of the symmetry. The dashed circle shows the outer radius of the hydrodynamical simulation. If the particle is within the radius, we use the gas velocity and density obtained from the hydrodynamical simulation. On the other hand, the particle is out of the radius, and we use the gas velocity and density that are the same as the outer boundary conditions of the hydrodynamical simulation.

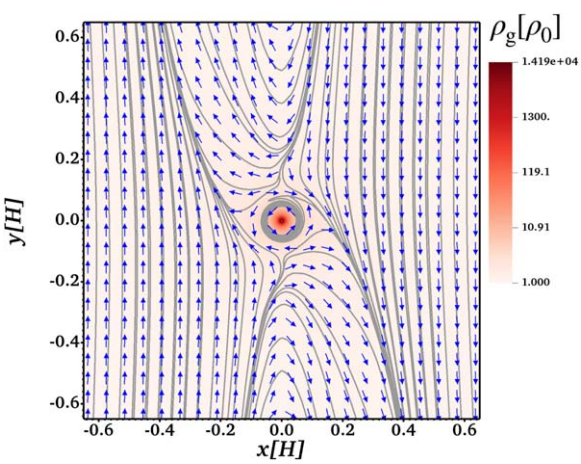

Figure 2. Flow patterns in the midplane ($z = 0$) for $m = 0.1$ at $t = 150\ \Omega^{-1}$ are shown by blue arrows and streamlines. The lengths of the arrows do not scale to the gas velocity. Color contour shows the gas density.

quasi-steady state, the density profile reaches the solution of the isothermal hydrostatic equilibrium in the 1D analysis (see derivation in Appendix A). It should be noted that the density enhancement around the planet occurs even for $r \gtrsim 0.1H \approx 0.3R_{\rm H} \approx R_{\rm B}$. Although the outer boundary of an atmosphere is conventionally set to the smaller of $R_{\rm H}$ and $R_{\rm B}$ (e.g., Inaba & Ikoma 2003), the atmospheric density enhancement occurs at $r \lesssim R_{\rm H}$ even if $R_{\rm H} > R_{\rm B}$.

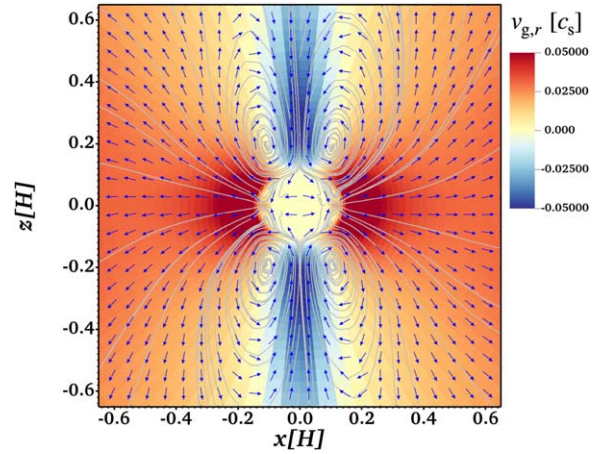

Figure 3. Flow patterns in the x–z plane ($y = 0$) for $m = 0.1$ at $t = 150\ \Omega^{-1}$ are shown by blue arrows and streamlines. The lengths of the arrows do not scale to the gas velocity. Color contour shows the velocity in the radial direction.

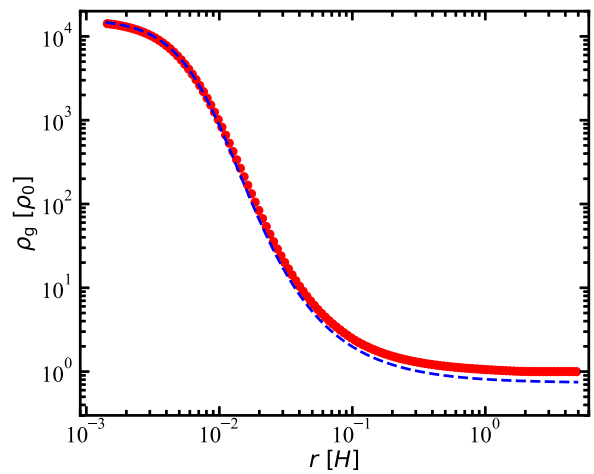

Figure 4. The gas density profile in the midplane ($z = 0$) for $m = 0.1$ is plotted as a function of distance from the center of the planet. The red circles show the gas density averaged over the azimuthal direction (ϕ) in the midplane for our numerical simulation. The blue dashed line corresponds to the analytical solution in Equation (A4).

In the simulation, the density profile of the atmosphere is determined by the hydrostatic equilibrium in the cooling model that we use. The profile is different from that for the growing planet, because the β cooling model is too simple. On the other hand, the cooling is effective in the vicinity of the planet. Once the closed flow pattern forms the atmosphere, the flow outside the atmosphere would be almost independent of the cooling. Taking into account our finding in the hydrodynamic simulations, we discuss the effect of the more realistic atmosphere in Section 5.2.

3.2. Two-dimensional Orbital Calculations

3.2.1. Example of 2D Orbits

First of all, we perform 2D orbital calculations in which particles have orbits in the midplane ($z = 0$). Figure 5 shows the trajectories of the particles with different St_0.

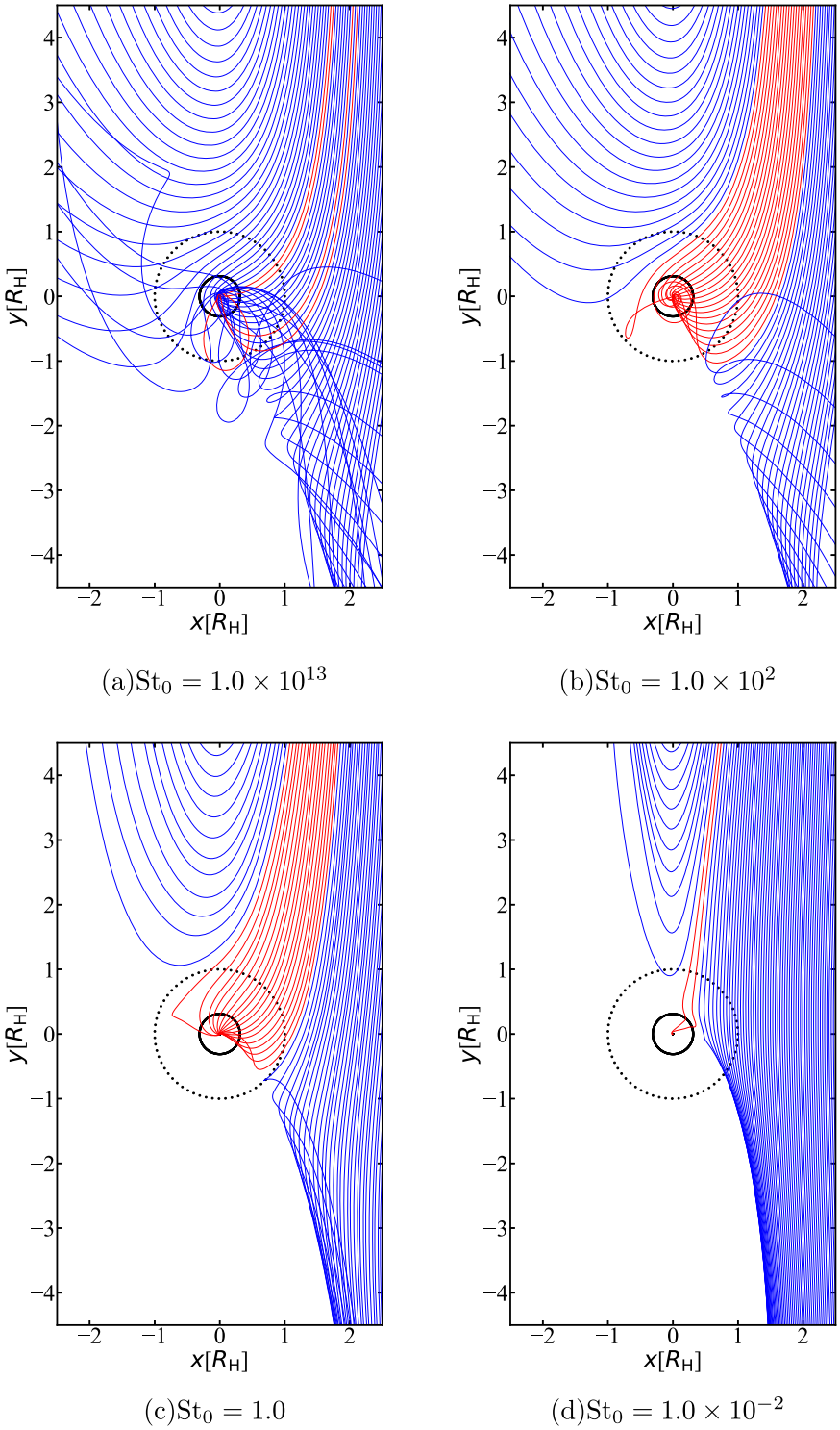

Figure 5. Trajectories of particles with different Stokes parameter for $m = 0.1$ are shown by solid lines. We restrict the motion of particles to 2D. The red and blue lines show the trajectories of particles that do and do not collide with the planet, respectively. The outer dotted and inner black circles are the Hill sphere and the Bondi sphere, respectively. The interval of orbits at the starting points is $0.01H$.

For the large Stokes parameter, $\mathrm{St}_0 = 1.0 \times 10^{13}$ (Figure 5(a)), the trajectories are almost the same as those in the gas-free case because particles are too large to be affected by the gas drag (Ida & Nakazawa 1989). Particles collide with the planet for the initial positions (x_s) in three discrete bands (Figure 5(a)).

For $\mathrm{St}_0 = 1.0 \times 10^2$ (Figure 5(b)), the orbits outside the Hill sphere are almost the same as those for $\mathrm{St}_0 = 1.0 \times 10^{13}$. However, the particles feel strong gas drag in the atmosphere. All the particles entering the Bondi sphere collide with the planet.

For $\mathrm{St}_0 \gg 1$, the orbits of particles are almost independent of St_0 and similar to the gas-free ones unless $r < R_{\mathrm{H}}$. In the Hill sphere, the velocities of particles can be larger than the sound velocity, and the gas density increases (see Figure 4). Therefore, gas drag effectively damps the kinetic energies of particles, which induces the capture of passing particles.

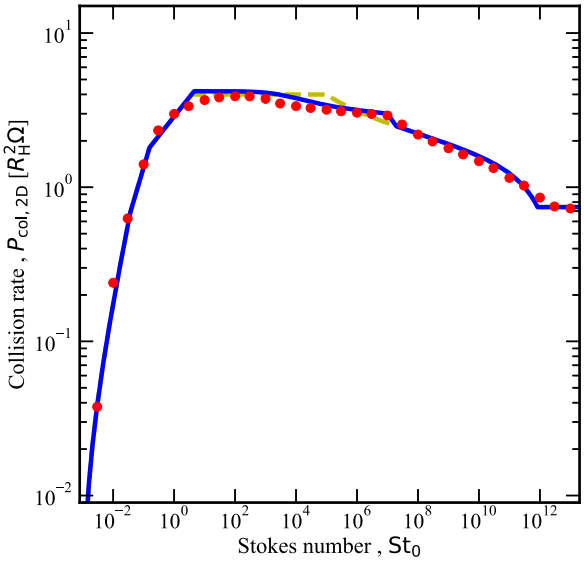

Figure 6. 2D specific collision rate, $P_{\rm col,2D}$, for $m = 0.1$ as a function of St_0 given by Equation (18). Red circles represent the collision rate obtained from the hydrodynamical and orbital calculations. The blue solid and yellow dashed lines indicate the detailed and simple analytical solutions given in Table 2, respectively.

For $\mathrm{St}_0 = 1.0$ (Figure 5(c)), the orbits of particles are similar to those for $\mathrm{St}_0 = 1.0 \times 10^2$. The orbits of particles in $y < 0$ are closer to the streamlines than those for $\mathrm{St}_0 = 10^2$ are. In addition, all particles entering the Hill sphere accrete onto the planet.

For $\mathrm{St}_0 = 1.0 \times 10^{-2}$ (Figure 5(d)), the orbits are almost same as the steady streamlines in Figure 2. The horseshoe width is much smaller than that for $\mathrm{St}_0 \gtrsim 1$. Particles are prevented from accreting onto the planet by the horseshoe flow and Keplerian shear flow, and the particles coming from the narrow band between the horseshoe and Keplerian shear flows are allowed to collide with the planet. This result is consistent with previous studies (Popovas et al. 2018; Homma et al. 2020; Kuwahara & Kurokawa 2020a, 2020b).

3.2.2. 2D Collision Rate

We calculate the 2D specific collision rate, $P_{\rm col} = P_{\rm col,2D}$, based on the orbital calculations. The definition of $P_{\rm col,2D}$ is given by

$$P_{\rm col,2D} = 2\int_0^\infty \Phi(x_{\rm s})|v_{0,y}|dx_{\rm s} = 3\Omega\int_0^\infty \Phi(x_{\rm s})x_{\rm s}dx_{\rm s}, \quad (20)$$

where $\Phi(x_{\rm s}) = 1$ if the particle collides with the planet and 0 otherwise, and $v_{0,y}$ is the y-component of the initial velocity in Equation (19). In order to account for the collision from both positive $x_{\rm s}$ and negative $x_{\rm s}$, we multiply the integral over positive $x_{\rm s}$ by 2.

Figure 6 shows the collision rate for $m = 0.1$ as a function of St_0. For $\mathrm{St}_0 \gtrsim 10^{12}$, the collision rate converges to a constant value, which is the same as the gas-free limit (Ida & Nakazawa 1989; Inaba et al. 2001).

For $\mathrm{St}_0 \gtrsim 1$, the collision rate increases with decreasing St_0. For large St_0, particles are scattered away owing to close encounters with the planet, so that $P_{\rm col,2D}$ is small. However, for small St_0, particles feel strong gas drag during close encounters because of high atmospheric density. Our hydrodynamical simulations indicate that density enhancement occurs even at $r \gtrsim R_{\rm B}$ if $r < R_{\rm H}$ (see Figure 4). For $1 \lesssim \mathrm{St}_0 \lesssim 10^2$, particles can be captured at the outer edge of the atmosphere, $r \sim R_{\rm H}$. In addition, a close encounter with the planet accelerates the velocity, which can exceed the sound velocity. The supersonic gas drag effectively reduces the kinetic energy prior to scattering. Particles are then captured by atmosphere, which enhances $P_{\rm col,2D}$ (Inaba & Ikoma 2003).

For $\mathrm{St}_0 \lesssim 1$, $P_{\rm col,2D}$ decreases with decreasing St_0. Small particles are well coupled to the gas. The flow pattern of the gas due to horseshoe and Keplerian shear limits the accretion of particles onto the planet (see Figure 5(d)). Therefore, the collision rate sharply decreases with decreasing St_0.

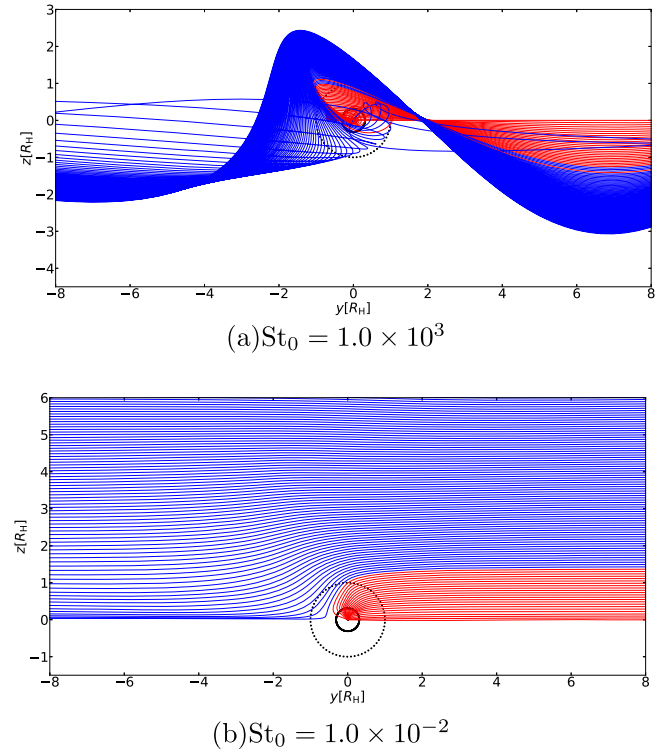

Figure 7. Trajectories of particles for different z_0 with interval 0.02 H projected on the y–z plane are shown by the solid lines for $\mathrm{St}_0 = 1.0 \times 10^3$ with $x_{\rm s} = 0.75\ H$ (panel (a)) and for $\mathrm{St}_0 = 1.0 \times 10^{-2}$ with $x_{\rm s} = 0.33\ H$ (panel (b)). The colors of solid lines and the outer dotted and inner circles are the same as in Figure 5. Note that the ranges of z are different in panels (a) and (b).

3.3. Three-dimensional Orbital Calculations

3.3.1. Example of 3D Orbits

First, we show the case of large particles (for $\mathrm{St}_0 > 1$). For $ia_{\rm s}$ or $z_0 \ll R_{\rm H}$, the 3D orbits projected on the x–y plane are almost the same as the 2D orbits. Figure 7(a) shows the orbits of particles projected on the y–z plane for $\mathrm{St}_0 = 1.0 \times 10^3$. For $i \gg R_{\rm H}/a_{\rm s}$, particles pass through the planet. Particles passing near the planet can be accreted onto the planet.

Figure 7(b) shows the orbits of the smaller particles projected on the y–z plane for $\mathrm{St}_0 = 1.0 \times 10^{-2}$. Particles can be accreted if they pass near the planet, as well as in the case of $\mathrm{St}_0 \gtrsim 1$.

3.3.2. 3D Collision Rate

We calculate the 3D specific collision rate. We then need the vertical distribution of particles for the calculation.

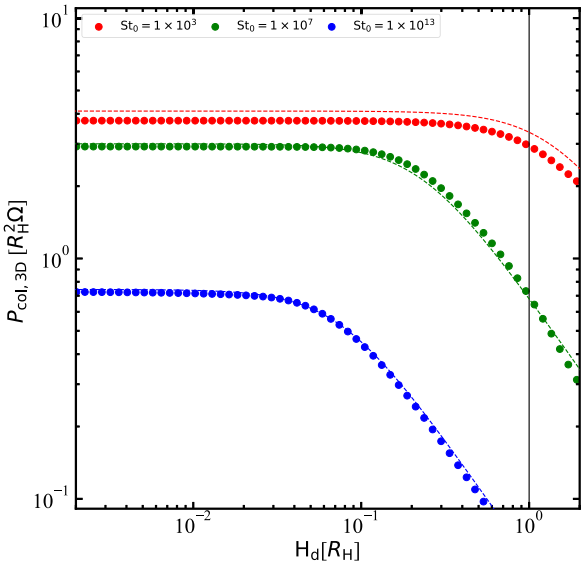

Figure 8. 3D specific collision rates, $P_{\rm col,3D}$, for $m = 0.1$ as a function of the particle scale height $H_{\rm d} = ai^*/\sqrt{2}$, where i^* is the dispersion of inclinations and a is the semimajor axis of the planet. Circles represent the collision rates obtained via the hydrodynamical and orbital simulations for $\mathrm{St}_0 = 10^3$ (red), 10^7 (green), and 10^{13} (blue). Dashed lines indicate the analytical solutions given in Table 2. The vertical solid black line is the Hill radius for reference.

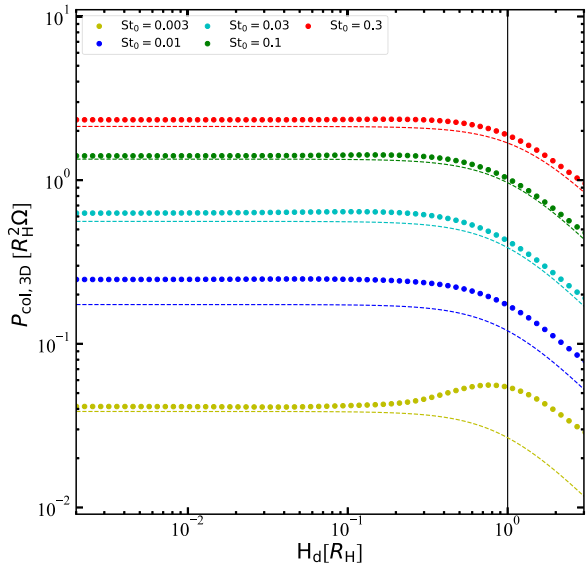

Figure 9. Same as Figure 8, but for $\mathrm{St}_0 < 1$.

For $\mathrm{St}_0 > 1$, we set the Rayleigh-type distribution for inclinations (Ida & Makino 1992). Assuming the random orbital phases, we obtain the collision rate as

$$P_{\rm col,3D}(i^*) = \frac{6\Omega}{\pi i^{*2}} \int_0^\infty \int_0^\pi \int_0^{z_{0,\max}/a_{\rm s}} \Phi(x_{\rm s}, i, \omega) x_{\rm s} i \times \exp\left(-\frac{i^2}{i^{*2}}\right) dx_{\rm s} d\omega di, \tag{21}$$

where i^* is the dispersion of i and $z_{0,\max}$ is the upper limit of z_0. Note that the vertical distribution of particles under this assumption corresponds to a Gaussian distribution for z_0 with the scale height of $a_{\rm s} i^*/\sqrt{2}$ (see Appendix B).

For $\mathrm{St}_0 < 1$, we assume the Gaussian distribution function of z_0. The collision rate is given by

$$P_{\rm col,3D}(H_{\rm d}) = \frac{3\Omega}{\sqrt{2\pi} H_{\rm d}} \int_0^\infty \int_0^\infty \Phi(x_{\rm s}, z_0) \times x_{\rm s} \exp\left(-\frac{z_0^2}{2H_{\rm d}^2}\right) dx_{\rm s} dz_0, \tag{22}$$

where $H_{\rm d}$ is the scale height of particles.

Figure 8 shows $P_{\rm col,3D}(i^*)$ for $\mathrm{St}_0 > 1.0$ as a function of $H_{\rm d} = a_{\rm s} i^*/\sqrt{2}$, using the relation between $H_{\rm d}$ and i^* given in Equation (B6). For $H_{\rm d} \ll R_{\rm H}$, $P_{\rm col,3D}$ is independent of $H_{\rm d}$ and almost the same as $P_{\rm col,2D}$. For $H_{\rm d} \gg R_{\rm H}$, $P_{\rm col,3D}$ decreases with $H_{\rm d}$. This is caused by the passing by without collisions for high-inclination particles (see Figure 7(a)).

Figure 9 shows $P_{\rm col,3D}(H_{\rm d})$ for $\mathrm{St}_0 < 1.0$. The dependence of $P_{\rm col,3D}$ on $H_{\rm d}$ is similar to that for $\mathrm{St}_0 > 1$. For $\mathrm{St}_0 = 0.003$, $P_{\rm col,3D}(H_{\rm d})$ increases around $H_{\rm d} = R_{\rm H}$. This increase is caused by the vertical gas flow that enters from high latitudes as seen in Figure 3 (see also Kuwahara & Kurokawa 2020a).

4. Analytic Formulae for $P_{\rm col}$

4.1. Analytic Formula of the 2D Collision Rate

In this subsection, we derive the analytic formulae for the 2D collision rate. The dominant effects determining the accretion rate depend on St_0. Therefore, we give different assumptions depending on St_0 to derive analytic formulae below. In Section 4.1.1, we introduce the previous study for the analytic formula without gas drag. In Section 4.1.2, we consider the atmospheric capture regime, where particles with $\mathrm{St}_0 \gtrsim 1$ entering atmospheres are captured owing to the energy losses by gas drag in atmospheres. In Section 4.1.3, we consider particles with $\mathrm{St}_0 \lesssim 1$ that settle down to a planet with terminal velocities during a close encounter with the planet. In Section 4.1.4, we consider particles with $\mathrm{St}_0 \ll 1$ that are strongly affected by the horseshoe and shear flows of gas.

4.1.1. Gas-free Limit

First, we confirm the analytic formula in the gas-free limit that means that particles and St_0 are extremely large. The 2D collision rate for the gas-free limit was derived in the previous studies, given by (Ida & Nakazawa 1989; Inaba et al. 2001)

$$\frac{P_{\rm col,free0}(R_{\rm pl})}{R_{\rm H}^2\Omega} = 11.3\sqrt{R_{\rm pl}/R_{\rm H}}, \tag{23}$$

where $R_{\rm pl}$ is the radius of the planet. This formula is in agreement with our simulations for the huge Stokes number. Note that Equation (23) is valid for $R_{\rm pl} \ll R_{\rm H}$. We improve the formula for $R_{\rm pl} \sim R_{\rm H}$ in Section 4.1.2.

4.1.2. Atmospheric Capture

Second, we derive the analytic formula for the atmospheric capture regime. Particles entering planetary atmosphere have high velocities owing to planetary gravity. We estimate the terminal velocity of particles at $r = R_{\rm B}$ as

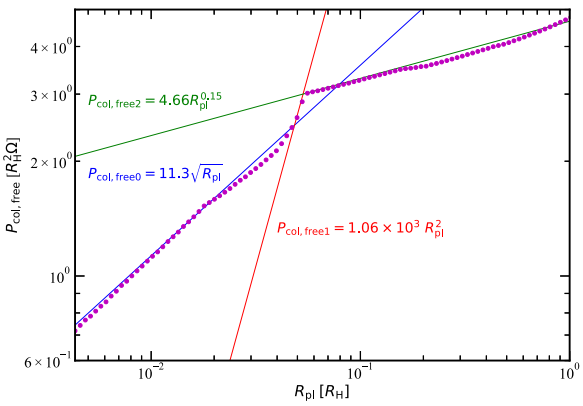

Figure 10. $P_{col,2D}$ is shown as a function of the planetary radius in the gas-free case.

$$u \sim \frac{GM_p}{R_B^2}\frac{St_0}{\Omega} = \frac{St_0}{m}c_s. \quad (24)$$

For $St_0 \gtrsim m$, the velocity can be greater than the sound velocity, so that the supersonic gas drag given by the second term in Equation (16) is effective in the atmosphere.

The kinetic energies of particles are damped by gas drag in the atmosphere. Once the particles' energies are smaller than the gravitational energy at the Hill radius, the orbits of the particles are bound by the planet. The kinetic energy at infinity is negligible. The condition for capture of particles is then given by

$$\Delta E < -\frac{GM_p m_p}{R_H}, \quad (25)$$

where ΔE is the energy loss due to gas drag in the atmosphere. We estimate ΔE from the integral of the energy loss along the particle orbit in the atmosphere with radius R_{atm}, given by

$$\Delta E(q) \approx -\zeta \int \pi r_p^2 \rho_{atm}(r) u^3\, dt = -4\zeta\pi G M_p r_p^2 \int_q^{R_{atm}} \frac{\rho_{atm}(r)}{\sqrt{r(r-q)}}\, dr, \quad (26)$$

where ζ is the number of close encounters between the planet and the particle and we assume a parabolic orbit with pericenter distance q for the particle, and then we use the relations $u^2 = 2GM_p/r$ and $dr/dt = \sqrt{2GM_p(r-q)}/r$ for the derivation. We multiply by 2 because the integral range is half of a parabola. The number of close encounters and the atmospheric radius are determined according to our simulation, and we adopt $\zeta = 2$ and $R_{atm} = 0.5\, R_H$. The following condition gives the captured radius R_{cap}:

$$\Delta E(R_{cap}) = -\frac{GM_p m_p}{R_H}. \quad (27)$$

We derive R_{cap} satisfying Equation (27).

According to Inaba & Ikoma (2003), we obtain P_{col} from $P_{col,free0}$ using R_{cap} instead of R_{pl}. However, $P_{col,free0}$ is valid for $R_{pl} \ll R_H$. Figure 10 shows the collision rate in the gas-free case as a function of the planetary radius. For $R_{pl} > 0.05 R_H$, we obviously need to modify the formula. Therefore, we give the collision rate

$$P_{col,free} = \mathrm{MIN}[\mathrm{MAX}(P_{col,free0}, P_{col,free1}), P_{col,free2}], \quad (28)$$

where

$$\frac{P_{col,free1}(R_{pl})}{R_H^2\Omega} = 1.06 \times 10^3 (R_{pl}/R_H)^2, \quad (29)$$

$$\frac{P_{col,free2}(R_{pl})}{R_H^2\Omega} = 4.66 (R_{pl}/R_H)^{0.15}. \quad (30)$$

For the atmospheric collision rate, we use R_{cap} instead of R_{pl} and then obtain

$$P_{col,atm} = P_{col,free}(R_{cap}). \quad (31)$$

4.1.3. Settling

Third, we derive the analytic formula for the settling regime. There are two regimes for settling: the cases of the supersonic gas drag, and the Stokes gas drag.

For $St_0 \lesssim 1$, Ormel & Klahr (2010) derived P_{col} for constant St in the Keplerian shear flow. They obtained the analytic formula by comparing the encounter time with the settling time. For a particle with an impact parameter x_s, the encounter time is estimated to be $t_{enc} = x_s/|v_{0,y}|$, where $|v_{0,y}| = 3\Omega x_s/2$ is the encounter velocity. The settling time needed for particles to settle down to the planet is given by $t_{set} = x_s/u_{term}$, where u_{term} is the terminal velocity determined by the force balance between the gravitational force and gas drag.

As explained above, for $St_0 \gtrsim m$, the velocity of the particle approaching the planet exceeds the sound velocity, so that the supersonic gas drag, the second term in Equation (16), is effective. The equation of force balance between the gravity and gas drag is given by

$$\frac{GM_p m_p}{r^2} = \pi r_p^2 \rho_g u_{term}^2, \quad (32)$$

so that the terminal velocity is expressed by

$$u_{term} = \sqrt{\frac{4GM_p\rho_p}{3\rho_g x_s^2}}\left(\frac{9\rho_g c_s l_{mfp}}{4\rho_p}\frac{St_0}{\Omega}\right)^{1/4}. \quad (33)$$

For $t_{enc} \gtrsim t_{set}$, particles are accreted onto the planets. The accretion condition is given as

$$C_1 \frac{x_s}{|v_{0,y}|} > \frac{x_s}{u_{term}}, \quad (34)$$

where C_1 is the constant value on the order of unity. The impact parameter x_s required for the settling is given by

$$x_s < x_{ss} = \left(\frac{8}{3}\right)^{1/4}\sqrt{C_1}\left(\frac{\rho_p}{\rho_g}\frac{c_s}{R_H\Omega}\frac{l_{mfp}}{R_H}St_0\right)^{1/8} R_H. \quad (35)$$

If x_{ss} is much larger than the half-width of the horseshoe orbit, P_{col} is given by

$$P_{col} = 3\Omega x_{ss}^2. \quad (36)$$

Using Equations (35) and (36), we obtain

$$\frac{P_{\rm col,ss}}{R_{\rm H}^2\Omega} = 2\sqrt{6}\,C_{\rm l}\left(\frac{\rho_{\rm p}}{\rho_{\rm g}}\frac{c_{\rm s}}{R_{\rm H}\Omega}\frac{l_{\rm mfp}}{R_{\rm H}}{\rm St}_0\right)^{1/4}. \tag{37}$$

On the other hand, if the terminal velocity of particles is smaller than the sound speed, we consider $\mathrm{St} \approx \mathrm{St}_0$ even in the encounter. In that case, the Stokes gas drag, the first term in Equation (16), is effective. The terminal velocity is given by

$$u_{\rm term} = \frac{GM_{\rm p}}{r^2}\frac{{\rm St}_0}{\Omega}. \tag{38}$$

Same as above, Equation (38) gives

$$x_{\rm ss} = (2C_{\rm l}{\rm St}_0)^{1/3}\,R_{\rm H}. \tag{39}$$

Using Equations (36) and (39), we obtain the collision rate,

$$\frac{P_{\rm col,set}}{R_{\rm H}^2\Omega} = 3(2C_{\rm l}{\rm St}_0)^{2/3}. \tag{40}$$

According to our simulations, $C_1 = 1.5$.

4.1.4. Effects of the Horseshoe and Outflow around the Bondi Radius

Finally, we derive the analytic formula considering the effects of the horseshoe and outflow around the Bondi radius. In our simulation, the outflow with a few percent of the sound speed is found around the Bondi radius, as shown in the previous study (Kuwahara et al. 2019). For smaller St_0, the horseshoe and outflow around the Bondi radius are effective. The collision rate is then given by $P_{\rm col} = 2\Delta x_{\rm s}|v_{0,y}|$, where $\Delta x_{\rm s} = |x_{\rm ss} - r_{\rm HS}|$ is the difference between the impact parameter and the half horseshoe width $r_{\rm HS}$. The particles passing around $r \sim R_{\rm B}$ are accreted onto the planet if they can enter the Bondi radius (see Figure 5(d)). We consider the passing particles are distributed from $r = R_{\rm B}$ to $r = R_{\rm B} + \Delta r$. The mass conservation gives $\Delta x_{\rm s}|v_{0,y}| = \Delta r v_\theta$. If the particle at $r = R_{\rm B} + \Delta r$ enters the Bondi radius with the radial drift of Δr during the encounter, the particle then accretes onto the planet. Therefore, the accretion condition is given by the passing time comparable to or longer than the drift time: $R_{\rm B}/v_\theta \gtrsim \Delta r/v_r$. We thus estimate $P_{\rm col}$ as

$$P_{\rm col} = 2R_{\rm B}v_r. \tag{41}$$

Assuming the outflow velocity of $\xi c_{\rm s}$ with $\xi \ll 1$, v_r is expressed by the terminal velocity $u_{\rm term}$ and the outflow velocity $\xi c_{\rm s}$, given by

$$v_r = \frac{GM_{\rm P}}{r^2}\frac{{\rm St}_0}{\Omega} - \xi c_{\rm s}. \tag{42}$$

Using Equations (41) and (42), we obtain

$$\frac{P_{\rm col,ho}}{R_{\rm H}^2\Omega} = 2\frac{R_{\rm B}}{R_{\rm H}}\left[\frac{3{\rm St}_0}{(R_{\rm B}/R_{\rm H})^2} - \xi\sqrt{\frac{3}{(R_{\rm B}/R_{\rm H})}}\right]. \tag{43}$$

We adopt $\xi = 0.1m$, based on the results of hydrodynamical simulations for $m = 0.03 - 0.1$. Note that the radial outflow velocity determined by ξ is much smaller than the flow velocity around $r \sim R_{\rm B}$ derived by Kuwahara et al. (2019). We use the m dependence of ξ given by their formula.

Table 2
Summary of Calculating the Analytic Collision Rate

$P_{\rm col,\ 2D}$	
1. Determine the size or stopping time of a particle:	Equation (18)
2. Calculate the capture radius $R_{\rm cap}$:	Equations (26) and (27)
3. Calculate $P_{\rm col,2D}$ in different regimes:	$P_{\rm col,atm}$ Equation (47) or Equation (51)
	$P_{\rm col,ss}$ Equation (48)
	$P_{\rm col,set}$ Equation (49)
	$P_{\rm col,ho}$ Equation (50)
4. Result of $P_{\rm col,2D}$:	$P_{\rm col,2D} = \mathrm{MIN}(P_{\rm col,atm}, P_{\rm col,ss}, P_{\rm col,set}, P_{\rm col,ho})$
$P_{\rm col,3D}$	
5. Determine the distribution of particles:	i^* or $H_{\rm d}$ ($i^* = \sqrt{2}H_{\rm d}/a$)
6. Calculate the impact parameter $x_{\rm ss}$:	Equation (35) if $P_{\rm col,2D} = P_{\rm col,ss}$
	Equation (39) if $P_{\rm col,2D} = P_{\rm col,set}$
	$x_{\rm ss} = 2R_{\rm B}$ if $P_{\rm col} = P_{\rm col,ho}$
7. Result of $P_{\rm col\ ,3D}$:	Equation (52) if $P_{\rm col,2D} = P_{\rm col,atm}$
	Equation (53) otherwise

4.2. Analytic Formulae of 3D Collision Rates

In this subsection, we focus on the 3D specific collision rate.

For $\mathrm{St}_0 > 1$, the i^* dependence of $P_{\rm col}$ is given in Inaba et al. (2001). Here, we consider the capture radius instead of the planetary radius according to Section 4.1.2 (e.g., Inaba & Ikoma 2003). We then obtain

$$\frac{P_{\rm col,3D}(i^*)}{R_{\rm H}^2\Omega} = \left\{\left(\frac{P_{\rm col,2D}}{R_{\rm H}^2\Omega}\right)^{-2} + \left[\frac{R_{\rm cap}^2}{4\pi a i^* R_{\rm H}}\left(17.3 + \frac{232\,R_{\rm H}}{R_{\rm cap}}\right)\right]^{-2}\right\}^{-1/2}, \tag{44}$$

where $R_{\rm cap}$ is the captured radius obtained from Equation (27).

For $\mathrm{St}_0 < 1$, $P_{\rm col,3D} \approx P_{\rm col,2D}$ for $H_{\rm d} \ll R_{\rm H}$, while $P_{\rm col,3D} \propto x_{\rm ss}/H_{\rm d}$ for $H_{\rm d} \gg R_{\rm H}$ (see Figure 9). Therefore, we empirically give

$$P_{\rm col,3D}(H_{\rm d}) = \left[(P_{\rm col,2D})^{-2} + \left(P_{\rm col,2D}\frac{x_{\rm ss}}{0.65H_{\rm d}}\right)^{-2}\right]^{-1/2}, \tag{45}$$

where $P_{\rm col,2D}$ is given by the smallest of Equations (37), (40), and (43) and $x_{\rm ss}$ is determined accordingly (see Table 2). If $P_{\rm col,2D}$ is given by Equation (43), we set $x_{\rm ss} = 2R_{\rm B}$.

Figures 8, 9, 11, and 12 show the analytical solution and simulation results. These formulae are in agreement with our simulation for almost all Stokes numbers, but for $\mathrm{St}_0 = 0.003$ in $m = 0.1$ the mean collision rate is underestimated for $H_{\rm d} \gtrsim R_{\rm H}$. This is the result of vertical gas flow that enters from high latitudes (Homma et al. 2020; Kuwahara & Kurokawa 2020a). This flow brings the particle that accretes onto the planet, so that the collision rate is maintained or increased.

4.3. Summary of Equations for P_{col}

In the following equations, we summarize the 2D collision rate,

$$P_{\rm col,2D} = \mathrm{MIN}(P_{\rm col,atm}, P_{\rm col,ss}, P_{\rm col,set}, P_{\rm col,ho}), \tag{46}$$

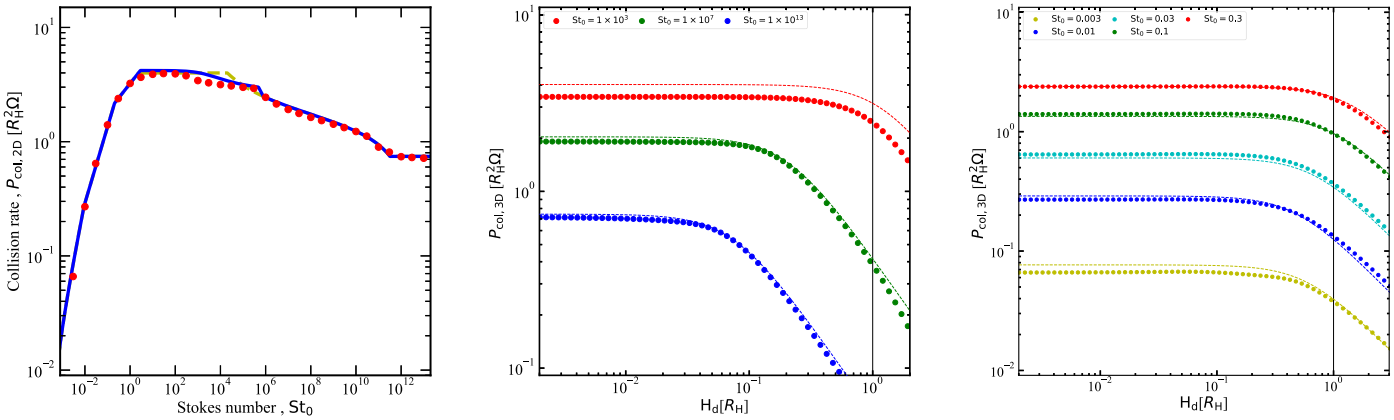

(a) $P_{\rm col,2D}$ (b) $P_{\rm col,3D}(i^*)$ (c) $P_{\rm col,3D}(H_{\rm d})$

Figure 11. Same as Figures 6, 8, and 9, but for $m = 0.05$.

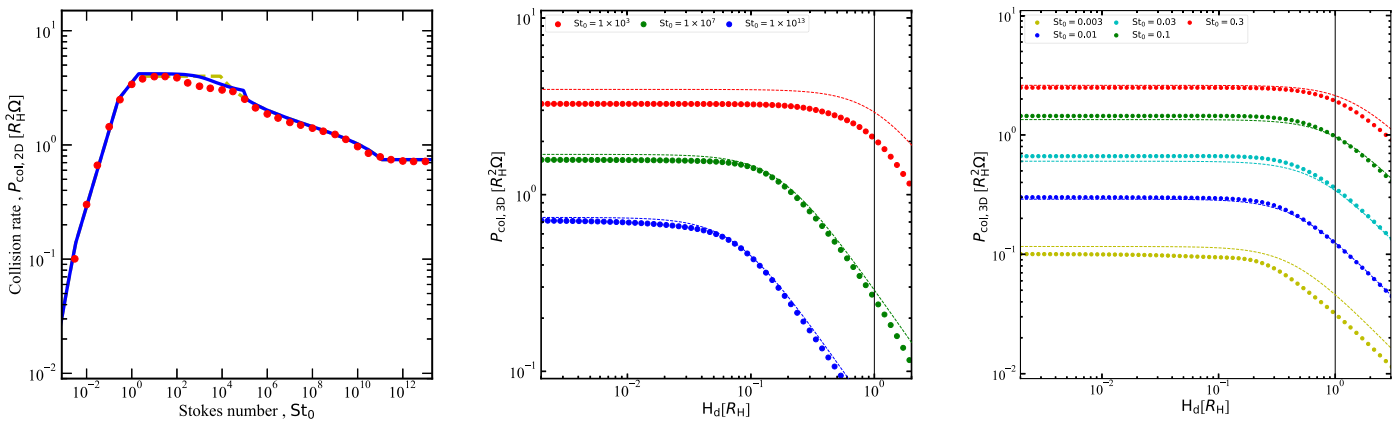

(a) $P_{\rm col,2D}$ (b) $P_{\rm col,3D}(i^*)$ (c) $P_{\rm col,3D}(H_{\rm d})$

Figure 12. Same as Figures 6, 8, and 9, but for $m = 0.03$.

where

$$P_{\rm col,atm} = P_{\rm col,free}(R_{\rm cap}), \tag{47}$$

$$\frac{P_{\rm col,ss}}{R_{\rm H}^2\Omega} = 2\sqrt{6}\,C_{\rm l}\left(\frac{\rho_{\rm p}}{\rho_{\rm g}}\frac{c_{\rm s}}{R_{\rm H}\Omega}\frac{l_{\rm mfp}}{R_{\rm H}}\mathsf{St}_0\right)^{1/4}, \tag{48}$$

$$\frac{P_{\rm col,set}}{R_{\rm H}^2\Omega} = 3(2C_{\rm l}\mathsf{St}_0)^{2/3}, \tag{49}$$

$$\frac{P_{\rm col,ho}}{R_{\rm H}^2\Omega} = 2\frac{R_{\rm B}}{R_{\rm H}}\left[\frac{3\mathsf{St}_0}{(R_{\rm B}/R_{\rm H})^2} - \xi\sqrt{\frac{3}{(R_{\rm B}/R_{\rm H})}}\right], \tag{50}$$

and $P_{\rm col,free}(R_{\rm cap})$ is given in Equation (28). Figures 6, 11, and 12 show the analytical solution and simulation results for $m = 0.1$, 0.05, and 0.03, respectively. Our analytic formulae are in agreement with our simulation.

If you feel that the formula for $P_{\rm col,free}$ in $P_{\rm col,atm}$ is complicated, $P_{\rm col,atm}$ can be simplified by setting the planetary radius $R_{\rm pl}$ to the capture radius $R_{\rm cap}$ in Equation (23); thus,

$$\frac{P_{\rm col,atm}}{R_{\rm H}^2\Omega} = 11.3\sqrt{\mathrm{MIN}(R_{\rm cap}/R_{\rm H},\,1/8)}. \tag{51}$$

Although the maximum of $R_{\rm cap}$ is much larger than $R_{\rm H}/8$, the simple formula overestimates $P_{\rm col}$ for large $R_{\rm cap}$, so that we give the upper limit $R_{\rm cap} = R_{\rm H}/8$ in Equation (51). The simple formula is shown by the yellow dashed lines in Figures 6, 11, and 12 and is almost the same as the more accurate formula.

If the vertical distribution is wide enough ($H_{\rm d} \gtrsim R_{\rm H}$), we need the 3D specific collision rate $P_{\rm col,3D}$. For $\mathsf{St}_0 > 1$, $P_{\rm col,2D} \approx P_{\rm col,atm}$ and the vertical distribution of particles is determined by orbital inclinations i. For i^*, the dispersion of i, $P_{\rm col,3D}$ is given by

$$\frac{P_{\rm col,3D}(i^*)}{R_{\rm H}^2\Omega} = \left\{\left(\frac{P_{\rm col,2D}}{R_{\rm H}^2\Omega}\right)^{-2} + \left[\frac{R_{\rm cap}^2}{4\pi a i^* R_{\rm H}}\left(17.3 + \frac{232\,R_{\rm H}}{R_{\rm cap}}\right)\right]^{-2}\right\}^{-1/2}, \tag{52}$$

where i^* is related to the scale height $H_{\rm d}$ as $i^* = \sqrt{2}H_{\rm d}/a$ (see Equation (B6)). On the other hand, for $\mathsf{St}_0 < 1$, $P_{\rm col}$ is determined by $P_{\rm col,ss}$, $P_{\rm col,set}$, or $P_{\rm col,ho}$, and $P_{\rm col,3D}(H_{\rm d})$ is given by

$$P_{\rm col,3D}(H_{\rm d}) = \left[(P_{\rm col,2D})^{-2} + \left(P_{\rm col,2D}\frac{x_{\rm ss}}{0.65H_{\rm d}}\right)^{-2}\right]^{-1/2}, \tag{53}$$

where x_{ss} is given by Equation (35) if $P_{col,2D} = P_{col,ss}$, x_{ss} is given by Equation (39) if $P_{col,2D} = P_{col,set}$, and $x_{ss} = 2R_B$ if $P_{col,2D} = P_{col,ho}$.

We compare the analytic formula for $m = 0.1$, 0.05, and 0.03 in Figures 8, 9, 11, and 12. The formula is in agreement with simulations for $m = 0.03 - 0.1$.

Table 2 shows the summary of how the collision rate P_{col} can be obtained.

5. Discussion

5.1. Comparison with Previous Studies

We derive the analytic solutions for the collision rates. These formulae are improved compared to the previous studies, as explained below.

Large particles are captured via planetary atmosphere. Protoplanets larger than the Moon can have an atmosphere (e.g., Mizuno et al. 1978). Inaba & Ikoma (2003) obtained the analytic formula for P_{col} using the capture radius R_{cap} instead of the planetary radius R_{pl}. They set the atmospheric outer boundary as given by R_B if $R_B < R_H$. However, the hydrodynamical simulation shows that the atmospheric radius, inside which the density is enhanced, is given by the Hill radius rather than by the Bondi radius (see Figure 4), resulting in $R_{cap} \sim R_H$ for small particles. However, their formula overestimates P_{col} for $R_{cap} \sim R_H$, because Equation (23) is valid only for $R_{cap} \ll R_H$. As discussed in Section 4.1.2, we thus improve the formula for $R_{cap} \sim R_H$. On the other hand, Inaba & Ikoma (2003) considered a single encounter. Multiple encounters are important for $R_{cap} \sim R_{pl}$, so that we take into account the effect (see Equation (26)).

We consider the supersonic gas drag, as well as the Stokes gas drag. In the previous studies for $St_0 < 1$, mainly the Stokes or Epstein gas drag laws were considered for discussing the pebble accretion. However, the velocity of the particles can be greater than the sound velocity, so that the supersonic gas drag is effective (see Equation (24)). We derive the analytic solution for $St_0 \sim 1$ considering the supersonic gas drag. This solution enables smooth connection of analytic solutions, between the atmospheric and settling regimes.

For the even smaller particles ($St_0 \ll 1$), the flow pattern of the gas due to horseshoe and Keplerian shear limits the accretion of particles onto the planet, as pointed out in the previous studies (Popovas et al. 2018; Homma et al. 2020; Kuwahara & Kurokawa 2020a, 2020b). We derive the analytic solution, considering the flow effect. For the 3D case, the vertical gas flow enters from high latitudes. Thus, particles can accrete onto the planet from high latitudes. This 3D effect is also shown in the previous studies. Taking into account the effect, we derive the analytical formula for the vertical distribution dependence of P_{col} (see Section 4.2).

5.2. Collision Rate for Realistic Atmosphere

In our simulation, the density of the atmosphere is unrealistic because the density profile reaches the hydrostatic isothermal solution and becomes shallower in the vicinity of the planet owing to the softening. As shown above, the density profile is consistent with the hydrostatic equilibrium in $r \lesssim R_H$ (see Figure 4). Therefore, adopting the hydrostatic density profile of the atmosphere according to the accretion heating and the opacity, we then obtain realistic P_{col}. In this subsection, we calculate the analytic collision rate using the more realistic density profile for the atmosphere than that obtained by the simulation.

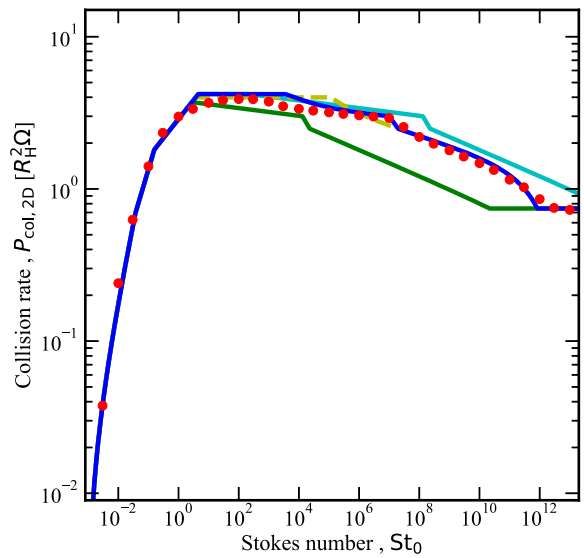

Figure 13. Same as Figure 6, but for the case of the more realistic atmosphere. The green and cyan lines correspond to the analytical solutions (Table 2) for $\kappa = 1$ cm^2 g^{-1} and $\kappa = 0.01$ cm^2 g^{-1}.

We consider low-opacity atmospheres, where the energy transportation is dominated by radiation rather than convection. For $r \ll R_B$, the analytical atmospheric density profile is approximately given by (Inaba & Ikoma 2003; Kobayashi et al. 2011)

$$\rho_{atm} = \frac{\pi\sigma_{SB}}{12\kappa L_e}\left(\frac{GM_p\mu m_H}{k_B}\right)^4 \frac{1}{r^3}, \tag{54}$$

where κ is the opacity of the atmosphere, k_B is the Boltzmann constant, and σ_{SB} is the Stefan–Boltzmann constant. The planetary luminosity L_e mainly comes from the accretion of bodies. We assume

$$L_e = \frac{GM_p}{R_{pl}}\frac{dM_p}{dt}. \tag{55}$$

We calculate R_{cap} according to the density profile given in Equation (54) and then obtain P_{col} from our analytic formula.

Figure 13 shows the analytical 2D specific collision rates (Table 2) for the more realistic density profile, assuming $dM_p/dt = 1 \times 10^{-6}\ M_\oplus\ \mathrm{yr}^{-1}$. The density profile in Equation (54) with $\kappa = 0.01$ cm^2 g^{-1} is similar to Equation (A4), so that the collision rate is similar to our simulation (Figure 13). For the planet formation, the accretion rate and P_{col} are determined consistently (e.g., Inaba et al. 2003; Chambers 2006; Kobayashi et al. 2011; Kobayashi & Tanaka 2018).

5.3. Estimate of Planetary Growth

In this subsection, we estimate the accretion timescale T_{acc} and the required disk mass M_{req} for the formation of a planet with mass M_p. Solid materials drift inward to the protoplanetary disk. The drift velocity v_{drift} is given by (Adachi et al. 1976; Weidenschilling 1977b)

$$v_{drift} = -\frac{2St_0}{1 + St_0{}^2} v_{hw}, \tag{56}$$

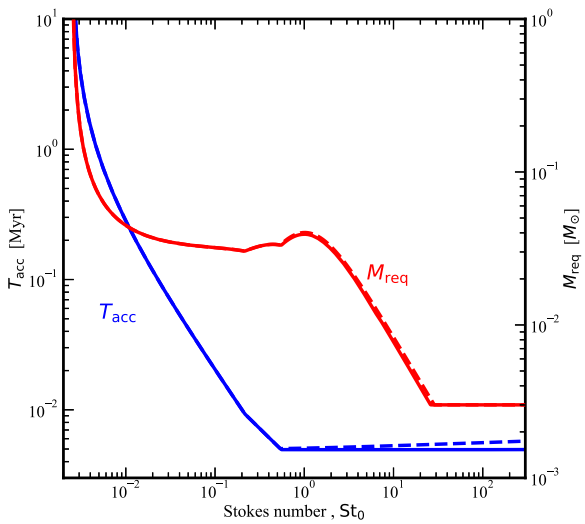

Figure 14. Blue and red lines show the accretion timescale and the required disk mass for $\kappa = 0.01$ cm^2 g^{-1} (solid) and 1 cm^2 g^{-1} (dashed). Note that our analytic formulae are applicable for $St_0 \lesssim 100$ (see Appendix C).

where v_{hw} is the headwind velocity. We define the accretion efficiency of solids

$$\varepsilon \equiv \frac{\dot{M}_p}{\dot{M}_{drift}} = \frac{P_{col}\Sigma_d}{2\pi a \Sigma_d |v_{drift}|}, \tag{57}$$

where Σ_d is the surface density of solids. The required disk mass and the accretion timescale are, respectively, defined by

$$M_{req} \equiv \frac{\chi M_p}{\varepsilon}, \tag{58}$$

$$T_{acc} \equiv \frac{M_p}{\dot{M}_p}. \tag{59}$$

where χ is the gas-to-solid ratio. We assume that the particle scale height is given by (Youdin & Lithwick 2007)

$$H_d = \left(1 + \frac{St_0}{\alpha}\frac{1 + 2St_0}{1 + St_0}\right)^{-1/2} H, \tag{60}$$

where α is the turbulent parameter (Shakura & Sunyaev 1973).

Figure 14 shows T_{acc} and M_{req} for a planetary mass $M_p = 10\ M_\oplus$, $a = 5$ au, $\Sigma_d = 2$ g cm^{-2}, $v_{hw} \approx 50$ m s^{-1}, $\chi = 100$, and $\alpha = 1 \times 10^{-3}$. We obtain P_{col} via the analytic formula shown in Table 2 for low-eccentricity particles. Therefore, our estimate is valid for $St_0 \lesssim 100$ (see Appendix C).

Very small particles ($St_0 \lesssim 10^{-3}$) are hardly accreted onto the planet (see Section 4.1.4), so that the accretion timescale and required mass are huge.

For $St_0 \sim 1$, the accretion timescale is much shorter than the disk lifetime as the previous studies have shown (e.g., Ormel & Klahr 2010). However, a massive disk is required for the formation of the single core of a gas giant planet.

For large particles ($St_0 \gtrsim 10$), the accretion timescale is as short as that for $St_0 \sim 1$, because of the atmospheric enhancement. The accretion efficiency is close to unity because the drift velocity is slow. The required disk mass is thus a constant value: $M_{req} \approx \chi M_p$ because of $\varepsilon \approx 1$.

The radial drift of particles with $St_0 \sim 1$ effectively supplies materials for planet growth in the inner disk. However, the accretion efficiency of such particles is low. Once collisional growth among drifting particles results in large bodies with $St_0 \gtrsim 10$, the cores of giant planets are effectively formed. We will address this issue by treating the collisional evolution and radial drift consistently (e.g., Kobayashi & Tanaka 2018).

6. Summary and Conclusions

In this paper, we investigate the effect of the protoplanetary disk perturbed by the planet on the collision rate of particles with the planet. We perform the nonisothermal 3D hydrodynamical simulation in the frame corotating with the planet and then integrate the equation of motion of particles in the gas flow obtained from the simulation considering the supersonic and Stokes gas drag. We then derive the new analytic formulae for the collision rate, considering the following regimes:

1. Meter-sized or larger particles are captured via the planetary atmosphere. Because they approach the planet exceeding the sound velocity, they feel strong gas drag. The atmosphere decelerates and captures the particles. The collision rate is significantly enhanced by the atmosphere.
2. Smaller particles are influenced by the gas flow in the protoplanetary disk effectively. They are well coupled to the gas flow. The collision rates are determined by comparing two timescales: the encounter timescale in which a particle has a close encounter with a planet, and the settling timescale in which a particle drifts onto a planet. If the settling timescale is shorter than the encounter timescale, a particle collides with a planet. For relatively large particles, the drift velocity is determined by the supersonic gas drag, while the Stokes gas drag is dominant for smaller particles.
3. If the particles are very small, the horseshoe gas flow and the outflow around the planet prevent particles from colliding with the planet. As a result, the collision rate sharply decreases with the decreasing size of particles. Particles can collide with the planet in the narrow band between the Keplerian shear and horseshoe flows.

These analytical formulae (summarized in Table 2) are in good agreement with our numerical simulations. In the 3D case, we also derive the analytic formulae (Equations (52) and (53)) and confirm the consistency between simulations and the analytical solutions. We show the method to obtain the analytic collision rate with the analytic formulae in Table 2 and Section 4.3.

We estimate the formation timescale of a solid core for the gas giant formation (Figure 14). The formation timescale is much shorter than the disk lifetime if $St_0 = 10^{-2}$ to 10^2. However, the drift velocity is so high that the accretion efficiency is small for $St_0 \lesssim 10$. Therefore, the collisional evolution between pebbles drifting from the outer disk may be important to reconcile the issue. Our results are helpful to discuss the planet formation in a wide size distribution of bodies.

We are grateful to the anonymous referee for helpful comments, which significantly improved the original version of our manuscript. We would like to thank Elijah Mullens for valuable comments. This work is supported by JSPS KAKENHI grant Nos. 17K05632, 17H01103, 17H01105, 18H05438, 18H05436, 20H04612, and 21K03642. Hydrodynamical simulations in this work were carried out on the Cray XC50 supercomputer at the Center for Computational

Astrophysics, National Astronomical Observatory of Japan. We thank Athena++ developers: James M. Stone, Kengo Tomida, Christopher White, and Kyle Gerard Felker.

Appendix A
Analytical Solution of the Density Profile

In our hydrodynamical simulations, we adopt the β cooling model. The density profile reaches the isothermal solution in the quasi-steady state. To solve the density profile analytically, we assume the hydrostatic equilibrium in the isothermal case. The equation for the hydrostatic equilibrium is given by

$$\frac{\partial p}{\partial r} = -\frac{GM_{\rm p} r}{(r^2 + r_{\rm s}^2)^{3/2}}\rho_{\rm g}. \tag{A1}$$

We use the relation between the density and the pressure in the isothermal, $p = \rho_{\rm g} c_{\rm s}^2$. We then have

$$\frac{1}{p}\frac{\partial p}{\partial r} = -\frac{R_{\rm B} r}{(r^2 + r_{\rm s}^2)^{3/2}}. \tag{A2}$$

The solution to this equation is given by

$$p = p_0 \exp\left(\frac{R_{\rm B}}{\sqrt{r^2 + r_{\rm s}^2}} - \frac{R_{\rm B}}{\sqrt{R_{\rm H}^2 + r_{\rm s}^2}}\right), \tag{A3}$$

$$\rho_{\rm g} = \rho_0 \exp\left(\frac{R_{\rm B}}{\sqrt{r^2 + r_{\rm s}^2}} - \frac{R_{\rm B}}{\sqrt{R_{\rm H}^2 + r_{\rm s}^2}}\right), \tag{A4}$$

where we assume $p = p_0$, $\rho_{\rm g} = \rho_0$ at the Hill radius.

The solution is plotted in Figure 4 and in agreement with our simulation.

Appendix B
Relation between the Dust Scale Height and the Dispersion of Inclinations

The large particles have orbital inclinations, so that the z-coordinate is given by

$$z = ia \sin\theta_{\rm s}, \tag{B1}$$

where $\theta_{\rm s}$ is the true anomaly of the particle. Assuming the isotropic distribution of the true anomaly, the distribution function of z for an arbitrary i, $f(z)$, is given by

$$f(z) = \frac{1}{\pi}\frac{1}{dz/d\theta_{\rm s}} = \frac{1}{\pi ia \cos\theta_{\rm s}} = \frac{1}{\pi ia(1 - z^2/i^2a^2)^{1/2}}. \tag{B2}$$

The Rayleigh-type distribution function of inclination is given by

$$n(i) = \frac{2i}{i^{*2}}\exp\left(-\frac{i^2}{i^{*2}}\right). \tag{B3}$$

Thus, the distribution function of z is given by

$$\int_{z/a}^{\infty} f(z)n(i)di = \int_{z/a}^{\infty} \frac{2\exp(-i^2/i^{*2})}{a\pi i^{*2}(1 - z^2/i^2a^2)^{1/2}}di = \frac{1}{a\sqrt{\pi}\, i^*}\exp\left(-\frac{z^2}{i^{*2}a^2}\right). \tag{B4}$$

Equation (B4) corresponds to the Gaussian distribution of z. On the other hand, the Gaussian distribution function of z with the scale height $H_{\rm d}$ is given by

$$\frac{1}{\sqrt{2\pi}H_{\rm d}}\exp\left(-\frac{z^2}{2H_{\rm d}^2}\right). \tag{B5}$$

Comparing the two distribution functions in Equations (B4) and (B5), we obtain

$$H_{\rm d} = \frac{ai^*}{\sqrt{2}}. \tag{B6}$$

Appendix C
Condition for $e^* \lesssim R_{\rm H}/a$

We here estimate the dispersion of eccentricity for small particles around a planet according to Kobayashi et al. (2010, 2011). The eccentricity stirring rate due to the viscous stirring is given by (Ohtsuki et al. 2002)

$$\frac{de^{*2}}{dt} = n_{\rm M} a^2 \left(\frac{R_{\rm H}}{a}\right)^4 \langle P_{\rm VS}\rangle \Omega, \tag{C1}$$

where e^* is the dispersion of eccentricity, $\langle P_{\rm VS}\rangle$ is the dimensionless stirring rate, and $n_{\rm M}$ is the surface number density of protoplanets given by

$$n_{\rm M} = \frac{1}{2^{4/3}\pi\tilde{b}R_{\rm H}a}, \tag{C2}$$

where $\tilde{b} \simeq 10$ is a factor of the orbital separation of protoplanets (Kokubo & Ida 2002). On the other hand, the e^*-damping rate due to the gas drag is given by

$$\frac{de^{*2}}{dt} = -2\frac{e^*}{{\rm St}_0}\Omega. \tag{C3}$$

Gas drag effectively damps e^* of small particles, so that we adopt $\langle P_{\rm VS}\rangle = 73$ independent of e^* for $e^* \ll R_{\rm H}/a$. Thus, the equilibrium condition between the stirring and the damping gives

$$e^{*2} = \frac{(R_{\rm H}/a)^3\langle P_{\rm VS}\rangle\Omega\,{\rm St}_0}{2^{7/3}\pi\tilde{b}} \sim 0.46\left(\frac{R_{\rm H}}{a}\right)^3 \Omega\,{\rm St}_0. \tag{C4}$$

For the planet formation with $M_{\rm p} = 10\ M_\oplus$ ($R_{\rm H}/a \approx 0.02$), $e^* \lesssim R_{\rm H}/a$ for ${\rm St}_0 \lesssim 100$. Therefore, our estimate in Figure 14 is valid for ${\rm St}_0 \lesssim 100$.

ORCID iDs

Tatsuya Okamura https://orcid.org/0000-0002-7441-2361
Hiroshi Kobayashi https://orcid.org/0000-0001-8808-2132

References

Adachi, I., Hayashi, C., & Nakazawa, K. 1976, PThPh, 56, 1756
Béthune, W., & Rafikov, R. R. 2019, MNRAS, 488, 2365
Chambers, J. E. 2006, ApJL, 652, L133
Chapman, S., & Cowling, T. G. 1970, The Mathematical Theory of Non-uniform Gases. An Account of the Kinetic Theory of Viscosity, Thermal Conduction and Diffusion in Gases (Cambridge: Cambridge Univ. Press)
Chrenko, O., & Lambrechts, M. 2019, A&A, 626, A109
Cimerman, N. P., Kuiper, R., & Ormel, C. W. 2017, MNRAS, 471, 4662
Eshagh, M. 2005, JESP, 31, 1

Fehlberg, E. 1969, NASA Technical Report R-315, NASA
Fung, J., Artymowicz, P., & Wu, Y. 2015, ApJ, 811, 101
Fung, J., Zhu, Z., & Chiang, E. 2019, ApJ, 887, 152
Gammie, C. F. 2001, ApJ, 553, 174
Hayashi, C., Nakazawa, K., & Nakagawa, Y. 1985, in Protostars and Planets II, ed. D. C. Black & M. S. Matthews (Tuscon, AZ: Univ. Arizona Press), 1100
Homma, T., Ohtsuki, K., Maeda, N., et al. 2020, ApJ, 903, 98
Ida, S., & Makino, J. 1992, Icar, 96, 107
Ida, S., & Nakazawa, K. 1989, A&A, 224, 303
Inaba, S., & Ikoma, M. 2003, A&A, 410, 711
Inaba, S., Tanaka, H., Nakazawa, K., Wetherill, G. W., & Kokubo, E. 2001, Icar, 149, 235
Inaba, S., Wetherill, G. W., & Ikoma, M. 2003, Icar, 166, 46
Kobayashi, H., & Tanaka, H. 2018, ApJ, 862, 127
Kobayashi, H., Tanaka, H., & Krivov, A. V. 2011, ApJ, 738, 35
Kobayashi, H., Tanaka, H., Krivov, A. V., & Inaba, S. 2010, Icar, 209, 836
Kokubo, E., & Ida, S. 2002, ApJ, 581, 666
Kurokawa, H., & Tanigawa, T. 2018, MNRAS, 479, 635
Kuwahara, A., & Kurokawa, H. 2020a, A&A, 633, A81
Kuwahara, A., & Kurokawa, H. 2020b, A&A, 643, A21
Kuwahara, A., Kurokawa, H., & Ida, S. 2019, A&A, 623, A179
Lambrechts, M., & Johansen, A. 2012, A&A, 544, A32
Lambrechts, M., & Lega, E. 2017, A&A, 606, A146
Mizuno, H., Nakazawa, K., & Hayashi, C. 1978, PThPh, 60, 699
Moldenhauer, T. W., Kuiper, R., Kley, W., & Ormel, C. W. 2021, A&A, 646, L11
Ohtsuki, K., Stewart, G. R., & Ida, S. 2002, Icar, 155, 436
Ormel, C. W. 2013, MNRAS, 428, 3526
Ormel, C. W. 2017, in The Emerging Paradigm of Pebble Accretion, ed. M. Pessah & O. Gressel, Vol. 445 (Berlin: Springer), 197
Ormel, C. W., & Klahr, H. H. 2010, A&A, 520, A43
Ormel, C. W., Kuiper, R., & Shi, J.-M. 2015a, MNRAS, 446, 1026
Ormel, C. W., Shi, J.-M., & Kuiper, R. 2015b, MNRAS, 447, 3512
Popovas, A., Nordlund, Å., & Ramsey, J. P. 2019, MNRAS, 482, L107
Popovas, A., Nordlund, Å., Ramsey, J. P., & Ormel, C. W. 2018, MNRAS, 479, 5136
Shakura, N. I., & Sunyaev, R. A. 1973, A&A, 500, 33
Stone, J. M., Tomida, K., White, C. J., & Felker, K. G. 2020, ApJS, 249, 4
Tanigawa, T., Maruta, A., & Machida, M. N. 2014, ApJ, 784, 109
Visser, R. G., & Ormel, C. W. 2016, A&A, 586, A66
Weidenschilling, S. J. 1977a, Ap&SS, 51, 153
Weidenschilling, S. J. 1977b, MNRAS, 180, 57
White, C. J., Stone, J. M., & Gammie, C. F. 2016, ApJS, 225, 22
Youdin, A. N., & Lithwick, Y. 2007, Icar, 192, 588